Chemical Science

ROYAL SOCIETY OF CHEMISTRY

EDGE ARTICLE

View Article Online
View Journal | View Issue

Cite this: *Chem. Sci.*, 2024, **15**, 15170

All publication charges for this article have been paid for by the Royal Society of Chemistry

Received 12th June 2024
Accepted 27th August 2024

DOI: 10.1039/d4sc03854a

rsc.li/chemical-science

Efficient circularly polarized multiple resonance thermally activated delayed fluorescence from B,N-embedded hetero[8]helicene enantiomers†

Tingting Huang,‡[a] Li Yuan,‡[c] Xueying Lu,[a] Yupei Qu,[a] Cheng Qu,[a] Yincai Xu,*[a] You-Xuan Zheng*[c] and Yue Wang*[ab]

Helicene-based circularly polarized multiple resonance thermally activated delayed fluorescence (CP-MR-TADF) materials are promising for ultra-high-definition and 3D displays, but most of them encounter potential problems such as easy racemization during the thermal deposition process, low luminous efficiency, and low luminescence dissymmetry factor (g_{lum}), making the development of efficient circularly polarized organic light-emitting diodes (CP-OLEDs) a significant challenge. Here, we report a pair of CP-MR-TADF enantiomers with high-order B,N-embedded hetero[8]helicene, (*P*/*M*)-**BN-TP-ICz**, by fusing two MR chromophores, DtCzB and indolo[3,2,1-*jk*]carbazole (ICz). **BN-TP-ICz** exhibits green emission in toluene with a peak of 531 nm and a full-width at half-maximum (FWHM) of 36 nm. The optimized CP-OLEDs with enantiomers (*P*/*M*)-**BN-TP-ICz** exhibit green emission with peaks of 540 nm, FWHMs of 38 nm and Commission Internationale de L'Eclairage coordinates of (0.33, 0.65). Moreover, they showcase maximum external quantum efficiencies (EQEs) of 32.0%, with g_{EL}s of $+6.49 \times 10^{-4}$ and -7.74×10^{-4} for devices based on (*P*)-**BN-TP-ICz**- and (*M*)-**BN-TP-ICz**, respectively.

Introduction

Chirality is a ubiquitous phenomenon in nature, a fundamental property of chemical substances.[1] In the fields of chemistry and materials research, chiral small molecules–a long-standing sustainable development interest and subject–are deeply fascinating to scientists.[2] Chiral molecules can serve as important mediators for chirality, and its constituent factors mainly include point chirality, axial chirality, planar chirality, and helical chirality.[3] Helicenes, as the most representative molecules of helical chirality, are essentially polycyclic aromatic hydrocarbons (PAHs) formed with *ortho*-fused aromatic/hetero rings.[4] The large steric hindrance between their "head" and "tail" compels them to adopt a helical three-dimensional topology, thereby inducing the generation of helical chirality.[5] The intrinsic helical chirality and unique three-dimensional π-conjugated structure of molecules endow them with excellent circular dichroism (CD) and circularly polarized luminescence (CPL) characteristics.[6] Recently, helical chiral materials have demonstrated extraordinary research value and broad application prospects in the realm of optoelectronics, especially in circularly polarized organic light-emitting diodes (CP-OLEDs).[7]

With the increasing diversification of lifestyle and the continuous evolution of display technology, the development of ultra-high-definition (UHD) displays with a wide color gamut has become the focus of cutting-edge OLED displays.[8] Therefore, integrating CPL with high-color-purity multiple resonance thermally activated delayed fluorescence (MR-TADF) materials has become a prevalent trend to create CP-MR-TADF emitters with multiple figures-of-merit.[9] CP-MR-TADF materials can directly emit CPL, avoiding energy loss caused by the need for circular polarizers and quarter-wave plates, and they can reduce glare and enhance contrast, clarity, and expressiveness of images in practical applications. Furthermore, they address the issue of low color purity encountered with traditional CPL materials.[10] Currently, the actively researched helicene-type CP-MR-TADF materials are mainly focused on [6]helicene or even lower-order helicenes.[11] Higher-order helicenes can easily overcome the problem of the low energy barrier of racemization, thereby avoiding the risk of configuration instability during vacuum thermal deposition and significantly improving repeatability.[12] Additionally, the helical chiral π-conjugated system can participate in the distribution of frontier molecular orbitals (FMOs) of molecules, favoring π-electron flow, which

[a]*State Key Laboratory of Supramolecular Structure and Materials, College of Chemistry, Jilin University, Changchun 130012, P. R. China. E-mail: ycxu17@mails.jlu.edu.cn; yuewang@jlu.edu.cn*

[b]*Jihua Laboratory, 28 Huandao Nan Road, Foshan, 528200, Guangdong Province, P. R. China*

[c]*State Key Laboratory of Coordination Chemistry, Jiangsu Key Laboratory of Advanced Organic Materials School of Chemistry and Chemical Engineering, Nanjing University, Nanjing 210023, P. R. China. E-mail: yxzheng@nju.edu.cn*

† Electronic supplementary information (ESI) available. CCDC 2361156. For ESI and crystallographic data in CIF or other electronic format see DOI: https://doi.org/10.1039/d4sc03854a

‡ T. Huang and L. Yuan contributed equally to this work.

facilitates enhancement of optical rotation and luminescence dissymmetry factor (g_{lum}).[13]

The general approach for constructing high-order helicenes is to increase the number of benzene rings in the helicene,[14] which not only poses challenges to molecular synthetic methodology but also usually accelerates the intersystem crossing (ISC) process from the lowest singlet (S_1) to the lowest triplet (T_1) excited state, leading to the accumulation of non-radiative triplet exciton transition and a significant reduction in photoluminescence quantum yields (Φ_{PL}s). Additionally, the extended persistent π-conjugated structure may destroy the alternating distribution pattern of FMOs and lead to an unpredictable broadening of the emission spectrum or even an uncontrollable loss of TADF characteristics.[15] Therefore, it is an ongoing pursuit to develop CP-MR-TADF materials with narrow full-width at half-maximum (FWHM), high Φ_{PL}, decent g_{lum}, and high energy barrier of racemization from large-sized higher-order helicenes.[16]

Our group has implemented the edge-topology molecular-engineering strategy to expand the sub-resonance skeleton of MR molecules and successfully developed an efficient helicene-type CP-MR-TADF emitter BN-Py.[17] This work provides a molecular construction template and synthetic methodology for the subsequent development of helical chiral CP-MR-TADF materials. In this contribution, following the well-defined paradigm, we initially made a tentative work to introduce a pure carbon PAH into the star MR-TADF molecule DtCzB,[18] and constructed a hetero[7]helicene-type molecule, BN-DBC, with a moderate energy barrier of racemization (Scheme 1). It exhibits yellow emission with a peak of 548 nm, a broad FWHM of 44 nm, and a low Φ_{PL} of 55% in toluene solution. Unfortunately, it lacks TADF characteristics, limiting its electroluminescence (EL) performance in devices. Subsequently, we further stitched a unique MR chromophore with a rigid planar structure independent of the B,N-containing MR framework, indolo[3,2,1-*jk*]carbazole (ICz), with the DtCzB fragment to develop a CP-MR-TADF molecule with high-order B,N-embedded hetero[8]helicene, **BN-TP-ICz**, with a high energy barrier of racemization. It displays vivid green emission with a peak of 531 nm, a narrow FWHM of 36 nm, and a high Φ_{PL} of 93% in toluene solution. The optimized CP-OLEDs with enantiomers (*P*/*M*)-**BN-TP-ICz** exhibit green emission with peaks of 540 nm, FWHMs of 38 nm and Commission Internationale de L'Eclairage (CIE) coordinates of (0.33, 0.65). Moreover, they showcase maximum external quantum efficiencies (EQEs) of 32.0%, with electroluminescence dissymmetry factors (g_{EL}s) of $+6.49 \times 10^{-4}$ and -7.74×10^{-4} for devices based on (*P*)-**BN-TP-ICz** and (*M*)-**BN-TP-ICz**, respectively. The successful construction of **BN-TP-ICz** effectively provides a new perspective for the future research on high-order helicene-type CP-MR-TADF materials.

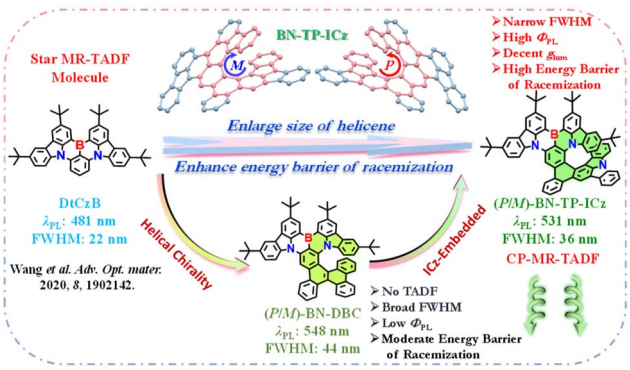

Scheme 1 Schematic diagram of molecular structure evolution of chiral hetero[*n*]helicene based on the parent molecule DtCzB and the corresponding photophysical properties.

Results and discussion

Synthesis and characterization

Both BN-DBC and **BN-TP-ICz** were prepared from the substrate DtCzB *via* the classic synthetic trilogy (Scheme S1†). DtCzB moiety was readily converted to DtCzB-Bpin through Miyaura borylation,[19] which then underwent Suzuki coupling with commercially available 9-(2-bromophenyl)fluorene and lab-synthesized 2-(2-iodophenyl)indolo[3,2,1-*jk*]carbazole (IP-ICz) (derived from 2-(4,4,5,5-tetramethyl-1,3,2-dioxaborolan-2-yl) indolo[3,2,1-*jk*]carbazole and 1-bromo-2-iodobenzene) to give the key precursors BN-PPhen and BN-P-ICz. Finally, hetero[7] helicene-embedded BN-DBC and hetero[8]helicene-embedded **BN-TP-ICz** were developed through intramolecular Scholl oxidative coupling. The main disparity in the synthetic procedures of these two target molecules lies in the oxidants adopted in the cyclization step, with the former employing iron(III) chloride, while the latter being induced by [bis(trifluoroacetoxy) iodo]benzene and boron trifluoride etherate. The molecular structures of all intermediates and target compounds were comprehensively characterized using NMR, mass spectrometry, and elemental analysis (Fig. S1–S7†). In addition, **BN-TP-ICz** exhibits outstanding thermal stability with a high decomposition temperature (T_d, corresponding to 5% weight loss) of 502 °C (Fig. S8†), which is advantageous for its application in vacuum thermal deposition OLEDs.

For comparison, the FMO distribution of BN-DBC was calculated (Fig. S9†), and its fundamental photophysical properties were characterized (Fig. S10, S11 and Table S1†). Compound BN-DBC in toluene solution (1×10^{-5} M) and PMMA (polymethyl methacrylate) film (1 wt% doping concentration) exhibits yellow emission with peaks of 548 and 553 nm, broad FWHMs of 44 and 50 nm, and low Φ_{PL}s of 55% and 60%, respectively. Furthermore, the lowest-excited singlet–triplet energy splittings (ΔE_{ST}s) were estimated to be 0.32 and 0.31 eV, respectively, which implies that BN-DBC likely does not exhibit TADF properties. The triplet spin density distribution (TSDD) is primarily on the dibenzo[*g*,*p*]chrysene group, which may reveal a substantial decrease in T_1 energy (Fig. S12†). Further analysis of the fluorescence lifetimes in toluene solution and PMMA doped film show mono-exponential transient photoluminescence (PL) decay with only nanosecond-scale prompt fluorescence detected (Fig. S13†). The combined theoretical calculations and experimental results indicate the absence of TADF properties in BN-DBC, which is therefore only used as a reference molecule and the properties are not further explored in this work. The associated experimental results of BN-DBC

demonstrate that it would be challenging to achieve the desired goals only by embedding a large-sized pure carbon PAH helicene into the MR-TADF molecule DtCzB.

A single crystal of racemic **BN-TP-ICz** was acquired *via* vacuum vapor-phase deposition (Fig. S14, S15 and Table S2†). Single-crystal X-ray crystallographic analysis reveals that the crystal **BN-TP-ICz** belongs to the triclinic crystal system and $P\bar{1}$ space group, and the π-conjugated framework consists of 54 sp^2 hybridized carbon atoms, 1 coordinated boron atom and 3 embedded nitrogen atoms ($C_{54}BN_3$), exhibiting an unequivocal non-planar hetero[8]helicene structure (Fig. 1a). Viewed from the side, the dihedral angle between the planes containing the DtCzB moiety and ICz moiety is 32.13°, giving **BN-TP-ICz** a highly folded and distorted conformation and exhibiting an angular two-dimensional topology. The bulky steric hindrance between ICz and DtCzB pulls and deforms the N–B–N-substituted central phenyl ring in DtCzB, forming a torsion angle of 30.49° (Fig. 1b). In the three-dimensional stacking structure of the crystal, **BN-TP-ICz** adopts a regular and dense linear strand arrangement along the *b*-axis, with two adjacent molecules of (*P*)- and (*M*)-enantiomers appearing in pairs, placed in an inverted manner (Fig. 1c). As a result, there are abundant π···π interactions in the crystal, including the π···π interactions between ICz planes of the paired molecules (*P*)-**BN-TP-ICz** and (*M*)-**BN-TP-ICz**, and the π···π interactions between DtCzB planes of molecule (*P*)-**BN-TP-ICz** and molecule (*M*)-**BN-TP-ICz** of the neighboring pair, with the distances of 3.571 and 3.363 Å, respectively.

Computational simulations

To gain an in-depth understanding of the geometrical structure and electronic characteristics of **BN-TP-ICz**, and considering that enantiomers have almost identical attributes except for chiroptical properties, (*P*)-**BN-TP-ICz** was selected for density functional theory (DFT) and time-dependent DFT (TDDFT) calculations. The highest occupied molecular orbital (HOMO) and lowest unoccupied molecular orbital (LUMO) distribution, HOMO–LUMO energy level gap (E_{gap}), and oscillator strength (*f*) of (*P*)-**BN-TP-ICz** are illustrated in Fig. 2a. In the optimized ground (S_0) state, (*P*)-**BN-TP-ICz** shows a highly distorted molecular conformation derived from the congested steric hindrance between DtCzB and ICz moieties. Due to the inherent MR characteristics of DtCzB and ICz, (*P*)-**BN-TP-ICz** generally retains the typical characteristics of the MR framework, with an alternating HOMO/LUMO distribution. The HOMO is predominantly localized on the nitrogen atoms and *ortho*/*para*-positions of the carbon atoms connected to nitrogen atoms in DtCzB moiety, while the LUMO is concentrated on the boron atom and *ortho*/*para*-positions of the carbon atoms connected to the boron atom in the DtCzB moiety, inducing a short-range charge transfer (SRCT) effect. In addition, the HOMO is partially extended to the ICz moiety, and the LUMO is partially diffused into the benzene ring connected to the *para*-carbon position of the B-substituted phenyl ring, inducing a long-range charge transfer (LRCT) effect.[20] This amalgamation of SRCT and LRCT states in (*P*)-**BN-TP-ICz** is not only anticipated to facilitate a bathochromic shift in the spectrum but also preserve the narrowband emission. The π-electron properties of (*P*)-**BN-TP-ICz** were analyzed with the localized orbital locator (LOL) function (Fig. S16†).[21] The results show that π-electrons in all-carbon benzene rings exhibit more pronounced six-center and six-electron delocalization than other rings, indicating a decent π-conjugation degree; in heterocycles containing boron or nitrogen atoms, π-electron flow is suppressed to some extent. Therefore, it can be concluded that the incorporation of heteroatoms significantly influences the molecular orbital distribution of the entire molecule and induces FMO separation. Furthermore, the hole–electron analysis map delineates well-separated holes and electrons in (*P*)-**BN-TP-ICz** (Fig. S17†).[22] The alternating distribution pattern of holes and electrons within the DtCzB fragment aligns with the alternating FMO distribution, indicating SRCT excitation from S_0 to S_1 state. In addition, the hole is also propagated into the ICz fragment, and the electron is also spread into the benzene ring connected to the *para*-carbon position of the B-substituted phenyl ring, facilitating LRCT excitation from S_0 to S_1 state.

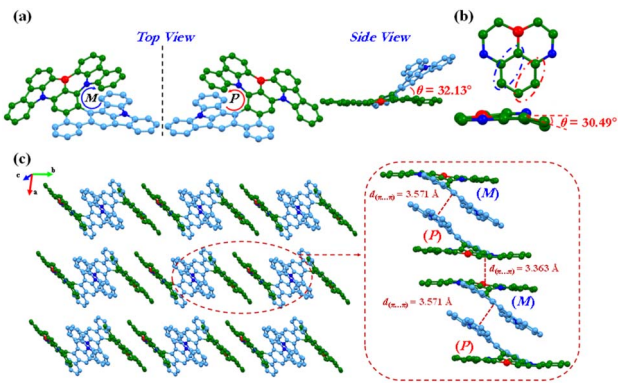

Fig. 1 Single crystal structure analysis of **BN-TP-ICz**. The ball and stick drawings of the top and side views are set, and all *tert*-butyl groups and hydrogen atoms are omitted for clarity. (a) Top/side view of **BN-TP-ICz** crystal structure, and the dihedral angle between ICz and DtCzB planes. (b) Torsion angle of the N–B–N-substituted central phenyl ring in DtCzB. (c) Stacking modes and π···π interactions.

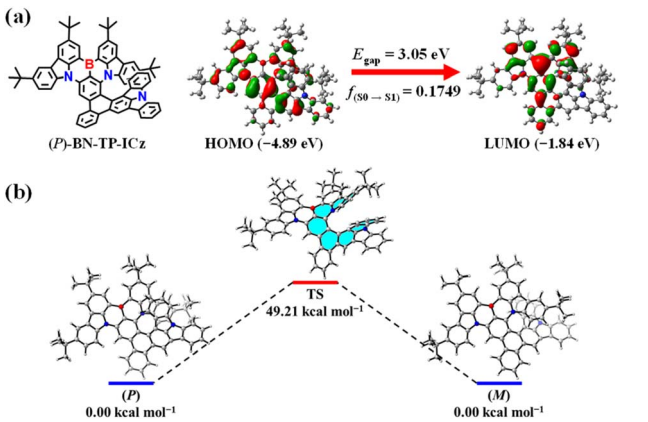

Fig. 2 (a) HOMO and LUMO distribution, HOMO–LUMO energy level gap, and oscillator strength of (*P*)-**BN-TP-ICz**. (b) Energy barrier of the racemization of enantiomers (*P*/*M*)-**BN-TP-ICz**.

Configurational stability is the paramount stereochemical feature of helicenes and their derivatives, which will directly impact their applications in chiroptics and optoelectronic devices. Therefore, we calculated the energy barrier of racemization of **BN-TP-ICz** (Fig. 2b).[23] Analysis of the transition states of (*P*/*M*)-**BN-TP-ICz** reveals an energy barrier of racemization up to 49.21 kcal mol^{-1}, which is higher than that of (*P*/*M*)-BN-DBC (37.25 kcal mol^{-1}, Fig. S18†), and is adequate to support chiral resolution and further research on chiroptical performances under thermal evaporation. Chiral resolution of **BN-TP-ICz** was favorably achieved, and a pair of enantiomers (*P*/*M*)-**BN-TP-ICz** with high optical purity were obtained (enantiomeric excess (ee) value >99.0%, Fig. S19†). The formation of the high energy barrier of racemization can be further elucidated by analyzing the intramolecular non-covalent interactions (NCIs) within (*P*)-**BN-TP-ICz** as a function of reduced density gradient (RDG) (Fig. S20†).[24] It is visually visible from the RDG isosurface that these NCIs are mainly concentrated in the spatial overlap region of head-to-tail rings of the hetero[8]helicene, demonstrating a robust steric hindrance effect that stems from the highly distorted and folded conformation of (*P*)-**BN-TP-ICz**. Consequently, during the configurational transition of (*P*/*M*)-**BN-TP-ICz**, overcoming these crowded steric hindrances becomes crucial, contributing to the high energy barrier of racemization of **BN-TP-ICz**.

Photophysical properties

Preliminary photophysical properties of **BN-TP-ICz** were characterized in toluene solution (1×10^{-5} M). Racemic **BN-TP-ICz** exhibits intense ultraviolet-visible (UV-vis) absorption peaking at 510 nm, attributed to a strong intramolecular charge transfer (ICT) transition excited state. It displays vibrant green fluorescence emission with a peak of 531 nm, a narrow FWHM of 36 nm, and CIE coordinates of (0.29, 0.66) (Fig. 3a and Table 1). The well-distinguishable mirror-symmetrical relationship between the absorption and emission spectra of **BN-TP-ICz**, along with a small Stokes shift of only 21 nm, indicates minimal geometric changes between S_0 and S_1 states. The fusion of DtCzB and ICz provides the molecular composite with a rigid framework, as evidenced by its root-mean-square deviation (RMSD) of 0.1507 Å (Fig. S21†) and low recombination energy of 0.22 eV (Fig. S22†). Furthermore, the rigid structure and MR effect endow the **BN-TP-ICz** molecule with a high Φ_{PL} of 93%. Utilizing fluorescence and phosphorescence spectra at 77 K (Fig. S23†), the ΔE_{ST} of **BN-TP-ICz** was estimated to be 0.19 eV, which is sufficient to provide a channel for the reverse intersystem crossing (RISC) process of triplet excitons and promote the formation of TADF. The HOMO and LUMO energy levels of **BN-TP-ICz** were estimated to be −5.06 and −2.69 eV, respectively (Fig. S24†).

Subsequently, the solid-state thin film of **BN-TP-ICz** doped in 9-(2-(9-phenyl-9*H*-carbazol-3-yl)phenyl)-9*H*-3,9′-bicarbazole (PhCzBCz) with 5 wt% doping concentration was prepared *via* vacuum thermal evaporation for further investigation of photophysical properties. The doped film of **BN-TP-ICz** emits green light with a peak of 540 nm and a FWHM of 43 nm (Fig. S25†).

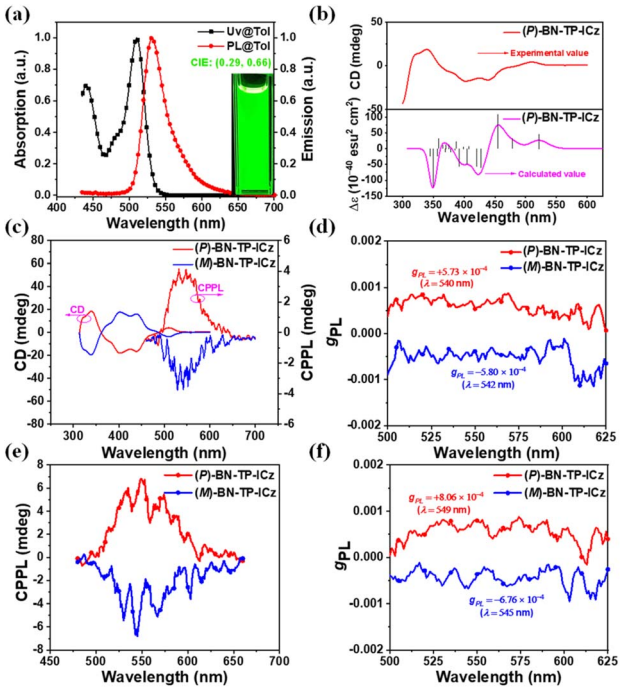

Fig. 3 (a) Normalized Uv-vis absorption and fluorescence spectra of **BN-TP-ICz**. (Inset: photograph taken under 365 nm UV light.) (b) Experimental and calculated CD spectra of (*P*)-**BN-TP-ICz**. (c) CD and CPPL spectra of (*P*/*M*)-**BN-TP-ICz**. (d) g_{PL} *vs.* wavelength curves of (*P*/*M*)-**BN-TP-ICz**. ((a–d) Measured in toluene solution (1×10^{-5} M, 298 K)), (e) CPPL spectra and (f) g_{PL} *vs.* wavelength curves of 3 wt% doping concentration (*P*/*M*)-**BN-TP-ICz** in PhCzBCz deposited films.

The bi-exponential transient PL decay curve, composed of nanosecond and microsecond components, observed at room temperature and under a vacuum atmosphere (Fig. S26a†), exhibits typical TADF features of **BN-TP-ICz**. It demonstrates prompt fluorescence decay with a lifetime (τ_p) of 5.8 ns and delayed fluorescence decay with a lifetime (τ_d) of 138.5 μs. Moreover, it is observed from the temperature-dependent transient PL decay curves that both the intensity and proportion of the delayed fluorescence component significantly increase as the temperature increases from 80 to 320 K (Fig. S26b†), intuitively substantiating TADF properties. Derived from the photophysical data of the doped film, the calculated rate constants show that the rate constant of prompt fluorescence (k_F) of **BN-TP-ICz** is 13.2×10^7 s^{-1}, significantly higher than its rate constant of internal conversion (k_{IC}) of 1.15×10^7 s^{-1}, indicating that the non-radiative energy loss is small; the corresponding rate constant of RISC (k_{RISC}) is 0.61×10^4 s^{-1} (Table S3†). These characteristics are consistent with the general photophysical behavior of MR-TADF materials.

To assess the chiroptical properties of enantiomers (*P*/*M*)-**BN-TP-ICz** in S_0 and S_1 states, their CD and CPL spectra were studied. The absolute configurations of the two components separated by chiral high performance liquid chromatography (HPLC) were confirmed by comparing the experimentally tested and theoretically simulated CD spectra of (*P*)-**BN-TP-ICz** (Fig. 3b),[25] identifying the first and second fractions as (*M*)-**BN-**

Table 1 Summary of the photophysical properties of the compound **BN-TP-ICz**

Compound	λ_{abs} [a] [nm]	λ_{em} [b] [nm]	FWHM [c] [nm]	E_{S_1} [d] [eV]	E_{T_1} [e] [eV]	ΔE_{ST} [f] [eV]	E_g [g] [eV]	HOMO [h] [eV]	LUMO [h] [eV]	ϕ_{PL} [i] [%]
BN-TP-ICz	510	531	36	2.44	2.25	0.19	2.32	−5.06	−2.69	93

[a] Peak wavelength of the lowest energy absorption band. [b] Peak wavelength of the PL spectrum in toluene solution (1×10^{-5} M, 298 K). [c] Full-width at half-maximum. [d] Singlet energy estimated from the onset of the fluorescence spectrum in toluene solution (1×10^{-5} M, 77 K). [e] Triplet energy estimated from the onset of the phosphorescence spectrum in a frozen toluene matrix (1×10^{-5} M, 77 K). [f] $\Delta E_{ST} = E_{S_1} - E_{T_1}$. [g] Optical band gap estimated from the absorption edge of the UV-vis spectrum. [h] Determined from cyclic voltammetry using the formula: $E_{HOMO} = -(E_{ox} + 4.8)$ eV and $E_{LUMO} = -(E_{red} + 4.8)$ eV. [i] Absolute photoluminescence quantum yield measured with an integrating sphere in N_2-bubbling toluene solution (1×10^{-5} M, 298 K).

TP-ICz and (*P*)-**BN-TP-ICz**, respectively. The enantiomers (*P*/*M*)-**BN-TP-ICz** exhibit distinct mirror symmetry in both CD and circularly polarized photoluminescence (CPPL) spectra in toluene solution (Fig. 3c). In the higher energy absorption bands at 313–362 and 362–489 nm, the CD spectra display intense Cotton effects, which correspond to the intrinsic localized state absorption of B,N-embedded hetero[8]helicene. In the lower energy region between 489 and 541 nm, the weak Cotton effect originates from the chirality transfer from the B,N-embedded hetero[8]helicene to the chromophore DtCzB. The photoluminescence dissymmetry factors (g_{PL}s) of (*P*)-**BN-TP-ICz** and (*M*)-**BN-TP-ICz** in toluene solution are $+5.73 \times 10^{-4}$ and -5.80×10^{-4}, respectively (Fig. 3d). To date, helicene-based CPL emitters have attracted widespread attention. CPL brightness (B_{CPL}), as a comprehensive indicator parameter of CPL performance, can easily compare the CPL activity of different compounds. Here, we calculated the B_{CPL} of (*P*)-**BN-TP-ICz** and compared it with the representative single-helicene-based CPL emitters reported previously to fully grasp the overall research progress in this field (Table S6†).[26] The results show that (*P*)-**BN-TP-ICz** exhibits decent CPL performance. The CPPL spectra of enantiomers (*P*/*M*)-**BN-TP-ICz** in the thermally deposited doped film (temperature: <160 °C, pressure: $<5 \times 10^{-4}$ Pa, thickness: 100 nm) also showcase good mirror symmetry, with g_{PL}s of $+8.06 \times 10^{-4}$ and -6.76×10^{-4}, respectively (Fig. 3e and f). Next, the optical purity of the residual enantiomers (*P*/*M*)-**BN-TP-ICz** samples after thermal deposition was further examined. Chiral HPLC analysis reveals that the ee values (>99.0%) are essentially consistent with those of the samples without thermal deposition treatment (Fig. S27†), indicating no racemization during the vacuum thermal deposition process and excellent configurational stability. The above results experimentally validate the rationality of incorporating ICz into DtCzB to form the **BN-TP-ICz** molecule with B,N-embedded hetero[8]helicene to construct CP-MR-TADF materials, laying a solid foundation for further research on CP-OLEDs.

Device performances

The CP-OLEDs were fabricated *via* vacuum thermal deposition with the configuration of [ITO/TAPC (50 nm)/TCTA (5 nm)/PhCzBCz: *x* wt% (*P*/*M*)-**BN-TP-ICz** (30 nm)/TmPyPB (30 nm)/LiF (1 nm)/Al (100 nm) ($x = 3$, 5, 8)] (Fig. S28†). In this setup, Al and ITO (indium tin oxide) were used as the cathode and anode, respectively. To balance hole and electron mobility, TAPC (1,1-bis[(di-4-tolylamino)phenyl]cyclohexane) and TmPyPB (3,3′-[5′′-[3-(3-pridinyl)phenyl][1,1′:3′,1′′-terphenyl]-3,3′′-diyl]bispyridine) with excellent charge carrier transport properties were employed as the hole transporting layer (HTL) and electron transporting layer (ETL), respectively, while TCTA (tris(4-carbazolyl-9-ylphenyl)amine) acted as the electron blocking layer (EBL) to confine the exciton recombination zone. Additionally, PhCzBCz with a highly twisted configuration and high triplet energy ($E_{T_1} = 2.96$ eV) was identified as the host of the emitting layer (EML) to suppress intermolecular stacking quenching and ensure efficient energy transfer.[27] Fig. 4, S29† and Table 2 summarize a range of curves and parameters of devices, including EL spectra, EQE–luminance (*L*) curves, as well as curves depicting the correlation between current density (*J*), voltage (*V*), current efficiency (CE), power efficiency (PE), and luminance, providing a comprehensive evaluation of the holistic EL performances.

Owing to the similar photophysical properties of enantiomers (*P*/*M*)-**BN-TP-ICz**, they also exhibit almost the same EL

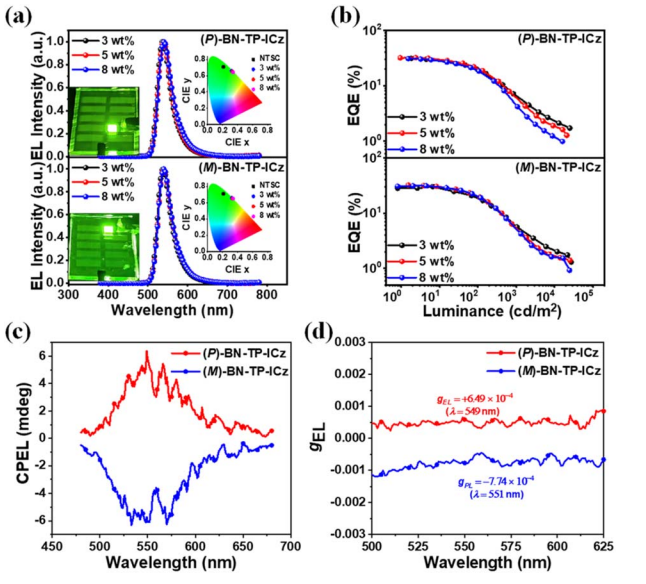

Fig. 4 EL spectra (a) and EQE–*L* curves (b) of the devices with the configuration of [ITO/TAPC (50 nm)/TCTA (5 nm)/PhCzBCz: *x* wt% (*P*/*M*)-**BN-TP-ICz** (30 nm)/TmPyPB (30 nm)/LiF (1 nm)/Al (100 nm) ($x = 3$, 5, 8)]. (Inset: color coordinates of the devices on the CIE 1931 color space, and photograph showing the emission color of the device with 3 wt% doping concentration.) CPEL spectra (c) and g_{EL} *vs.* wavelength curves (d) of the devices with the configuration of [ITO/TAPC (50 nm)/TCTA (5 nm)/PhCzBCz: 5 wt% (*P*/*M*)-**BN-TP-ICz** (30 nm)/TmPyPB (30 nm)/LiF (1 nm)/Al (100 nm)].

Table 2 Summary of EL data of devices (single host: PhCzBCz) based on emitters (*P*/*M*)-**BN-TP-ICz** with different doping concentrations

x wt%	λ_{em}[a] [nm]	FWHM[b] [nm]	CIE(x, y)[c]	V_{on}[d] [V]	L_{max}[e] [cd m^{-2}]	CE_{max}[f] [cd A^{-1}]	PE_{max}[g] [lm W^{-1}]	EQE[h] [%]
3 (A)	536	38	(0.32, 0.66)	3.1	25 180	130.0	131.7	31.1/19.5/6.6
5 (A)	540	38	(0.33, 0.65)	3.0	20 940	135.0	140.7	32.0/20.3/6.1
8 (A)	540	40	(0.34, 0.64)	3.0	16 240	123.8	129.7	30.7/18.6/4.5
3 (B)	540	38	(0.32, 0.66)	3.0	27 520	121.9	119.7	30.0/18.5/5.8
5 (B)	540	38	(0.33, 0.65)	3.0	25 450	128.7	134.8	32.0/20.1/5.3
8 (B)	540	39	(0.34, 0.65)	3.0	24 710	113.2	115.9	31.2/19.9/5.2

[a] EL peak wavelength. [b] Full-width at half-maximum. [c] Commission Internationale de L'Eclairage coordinates (value taken at 100 cd m^{-2}). [d] Turn-on voltage at 1 cd m^{-2}. [e] Maximum luminance. [f] Maximum current efficiency. [g] Maximum power efficiency. [h] Maximum external quantum efficiency, and values at 100 and 1000 cd m^{-2}, respectively. (Note: (A) denotes the device with (*P*)-**BN-TP-ICz**, (B) denotes the device with (*M*)-**BN-TP-ICz**.

performances in devices. All the single host-based devices demonstrate effective carrier injection and transport, with turn-on voltages (V_{on} at 1 cd m^{-2}) of ≤3.1 V. They achieve complete energy transfer at 3 wt% doping concentration, but the optimal EL performances are attained when the doping concentration increases to 5 wt%. At the optimal doping concentration, (*P*/*M*)-**BN-TP-ICz**-based devices show green emission with peaks of 540 nm and narrow FWHMs of 38 nm, and CIE coordinates of (0.33, 0.65). (*P*)-**BN-TP-ICz**- and (*M*)-**BN-TP-ICz**-based devices achieve maximum EQEs of 32.0% and 32.0%, maximum CEs of 135.0 and 128.7 cd A^{-1}, and maximum PEs of 140.7 and 134.8 lm W^{-1}, respectively, which are much better than those of the BN-DBC-based single-host device with an identical device structure at 5 wt% doping concentration (maximum EQE = 4.7%, CE = 17.2 cd A^{-1} and PE = 16.4 lm W^{-1}, Fig. S30† and Table S4†). The devices based on emitter (*P*/*M*)-**BN-TP-ICz** have remarkably maximum EQEs, principally because the EML PhCzBCz: 5 wt% **BN-TP-ICz** simultaneously has a high ϕ_{PL} of up to 92% (Table S3†) and dominant horizontal emitting dipole orientation ratio ($\Theta_{//}$) of up to 80% (Fig. S31†). The calculated $S_0 \rightarrow S_1$ transition dipole moment (TDM) of molecule (*P*)-**BN-TP-ICz** reveals that its TDM direction is mainly along the *x*-axis, and the TDM vector has a minor *Z* component (Fig. S32†), indicating that when anchored on the surface of a thin film, the emitter (*P*/*M*)-**BN-TP-ICz** may have a natural tendency to preferentially align the molecular axis horizontally. When the doping concentration increases to 8 wt%, the EL performances of the devices show an observable decrease, which is potentially attributed to molecular aggregation-induced quenching and confirmed by the appreciable crystal π⋯π stacking. Furthermore, the devices with 5 wt% doping concentration (*P*/*M*)-**BN-TP-ICz** exhibit good spectral stability with the increase in driving voltage (Fig. S33†), suggesting that there is only one stationary exciton recombination zone located in the EML within the device architecture, which is beneficial for its practical applications. More importantly, (*P*/*M*)-**BN-TP-ICz**-based devices with 5 wt% doping concentration shows distinct mirror circularly polarized electroluminescence (CPEL) spectra signal with decent g_{EL}s of +6.49 × 10^{-4} and −7.74 × 10^{-4} for (*P*)-**BN-TP-ICz** and (*M*)-**BN-TP-ICz**, respectively. In summary, (*P*/*M*)-**BN-TP-ICz**-based devices not only exhibit excellent EL performance but also show good CPEL characteristics, which verifies the scientificity of fusing ICz into DtCzB to construct CP-MR-TADF materials with B,N-embedded hetero[8]helicene, making their application in UHD CP-OLED displays attractive. In addition, since the efficiency roll-off of **BN-TP-ICz**-based devices is relatively large, the use of the sensitization strategy can alleviate the device efficiency roll-off to a certain extent.[28] Related research is provided in the ESI (Fig. S34–S37 and Table S5).†

Conclusions

In conclusion, we have successfully developed a pair of CP-MR-TADF enantiomers with a high-order B,N-embedded hetero[8]helicene, **BN-TP-ICz**. The molecule fuses two high-performance MR chromophores, DtCzB and ICz, which are endowed with the advantages of narrowband emission and high efficiency. The enantiomers (*P*/*M*)-**BN-TP-ICz** exhibit significant configurational stability and high energy barrier of racemization. The optimized CP-OLEDs based on single host PhCzBCz and enantiomers (*P*/*M*)-**BN-TP-ICz** demonstrate green emission with peaks of 540 nm, FWHMs of 38 nm, CIE coordinates of (0.33, 0.65), and maximum EQEs of 32.0%. Moreover, they showcase distinct mirror CPEL spectra signal with decent g_{EL}s of +6.49 × 10^{-4} and −7.74 × 10^{-4} for (*P*)-**BN-TP-ICz** and (*M*)-**BN-TP-ICz**, respectively. The successful construction of **BN-TP-ICz** not only enriches the structural diversity of MR-TADF materials, but also presents a straightforward and viable synthetic strategy for constructing large-sized helicene-type CP-MR-TADF materials with excellent configuration stability, which provides conceptual guidance for the construction of narrowband chiral emitters in future UHD CP-OLED displays.

Data availability

The datasets generated and/or analyzed during the current study are available from the corresponding author on reasonable request. The data include experimental results, characterization data, and any computational models used in the analysis. The following specific data types are available:

Raw and processed data: experimental measurements, including raw data from spectroscopic, NMR, and other characterization techniques.

ESI material†: additional information such as detailed experimental procedures, intermediate data, and supplementary figures.

Requests for data should be directed to [yuewang@jlu.edu.cn]. The data will be made available in a timely manner to ensure transparency and reproducibility of the results presented in this study.

Author contributions

Conceptualization, Yincai Xu; methodology, Tingting Huang and Li Yuan; validation, Yincai Xu, You-Xuan Zheng and Yue Wang; formal analysis, Yincai Xu and Tingting Huang and Li Yuan; investigation, Tingting Huang and Li Yuan; resources, Xueying Lu; data curation, Yupei Qu and Cheng Qu; writing – original draft, Tingting Huang and Yincai Xu; writing – review & editing, Yincai Xu; supervision, You-Xuan Zheng and Yue Wang.

Conflicts of interest

There are no conflicts to declare.

Acknowledgements

This work was supported by the National Natural Science Foundation of China (21935005 and 92256304), the National Key R&D Program of China (2020YFA0714601), Jihua Laboratory (X190321TF190) and Foshan Science and Technology Innovation Team Special Project (1920001000128).

Notes and references

1 M. Liu, L. Zhang and T. Wang, *Chem. Rev.*, 2015, **115**, 7304–7397.

2 (*a*) L. Frédéric, A. Desmarchelier, L. Favereau and G. Pieters, *Adv. Funct. Mater.*, 2021, **31**, 2010281; (*b*) P. Peluso and B. Chankvetadze, *Chem. Rev.*, 2022, **122**, 13235–13400.

3 J. R. Brandt, F. Salerno and M. J. Fuchter, *Nat. Rev. Chem*, 2017, **1**, 0045.

4 (*a*) E. VanderDonckt, J. Nasielski, J. R. Greenleaf and J. B. Birks, *Chem. Phys. Lett.*, 1968, **2**, 409–410; (*b*) Y. Shen and C. F. Chen, *Chem. Rev.*, 2012, **112**, 1463–1535.

5 K. Dhbaibi, L. Favereau and J. Crassous, *Chem. Rev.*, 2019, **119**, 8846–8953.

6 (*a*) J. A. Schellman, *Chem. Rev.*, 1975, **75**, 323–331; (*b*) D.-W. Zhang, M. Li and C.-F. Chen, *Chem. Soc. Rev.*, 2020, **49**, 1331–1343.

7 (*a*) M. Li, S.-H. Li, D. Zhang, M. Cai, L. Duan, M.-K. Fung and C.-F. Chen, *Angew. Chem., Int. Ed.*, 2018, **57**, 2889–2893; (*b*) L. Xu, H. Liu, X. Peng, P. Shen, B. Z. Tang and Z. Zhao, *Angew. Chem., Int. Ed.*, 2023, **62**, e202300492; (*c*) Z.-G. Wu, H.-B. Han, Z.-P. Yan, X.-F. Luo, Y. Wang, Y.-X. Zheng, J.-L. Zuo and Y. Pan, *Adv. Mater.*, 2019, **31**, 1900524; (*d*) S.-Y. Yang, Y.-K. Wang, C.-C. Peng, Z.-G. Wu, S. Yuan, Y.-J. Yu, H. Li, T.-T. Wang, H.-C. Li, Y.-X. Zheng, Z.-Q. Jiang and L.-S. Liao, *J. Am. Chem. Soc.*, 2020, **142**, 17756–17765; (*e*) J.-K. Li, X.-Y. Chen, Y.-L. Guo, X.-C. Wang, A.-C. Sue, X.-Y. Cao and X.-Y. Wang, *J. Am. Chem. Soc.*, 2021, **143**, 17958–17963.

8 (*a*) R. M. Soneira, *Inf. Disp.*, 2016, **32**, 26–31; (*b*) International Telecommunication Union, Recommendation ITU-R BT.2020, Parameter values for ultrahigh definition television systems for production and international program exchange, **https://www.itu.int/rec/R-REC-BT.2020-2-201510-I/en**.

9 (*a*) H. Uoyama, K. Goushi, K. Shizu, H. Nomura and C. Adachi, *Nature*, 2012, **492**, 234–238; (*b*) T. Hatakeyama, K. Shiren, K. Nakajima, S. Nomura, S. Nakatsuka, K. Kinoshita, J. Ni, Y. Ono and T. Ikuta, *Adv. Mater.*, 2016, **28**, 2777–2781; (*c*) Y. Xu, Q. Wang, X. Cai, C. Li and Y. Wang, *Adv. Mater.*, 2021, **33**, 2100652; (*d*) Z.-P. Yan, L. Yuan, Y. Zhang, M.-X. Mao, X.-J. Liao, H.-X. Ni, Z.-H. Wang, Z. An, Y.-X. Zheng and J.-L. Zuo, *Adv. Mater.*, 2022, **34**, 2204253; (*e*) X. Wu, J.-W. Huang, B.-K. Su, S. Wang, L. Yuan, W.-Q. Zheng, H. Zhang, Y.-X. Zheng, W. Zhu and P.-T. Chou, *Adv. Mater.*, 2022, **34**, 2105080; (*f*) Z. Chen, C. Zhong, J. Han, J. Miao, Y. Qi, Y. Zou, G. Xie, S. Gong and C. Yang, *Adv. Mater.*, 2022, **34**, 2109147; (*g*) Y. Kondo, K. Yoshiura, S. Kitera, H. Nishi, S. Oda, H. Gotoh, Y. Sasada, M. Yanai and T. Hatakeyama, *Nat. Photonics*, 2019, **13**, 678–682; (*h*) S.-Y. Yang, S.-N. Zou, F.-C. Kong, X.-J. Liao, Y.-K. Qu, Z.-Q. Feng, Y.-X. Zheng, Z.-Q. Jiang and L.-S. Liao, *Chem. Commun.*, 2021, **57**, 11041–11044; (*i*) W. Yang, N. Li, J. Miao, L. Zhan, S. Gong, Z. Huang and C. Yang, *CCS Chem.*, 2022, **4**, 3463–3471; (*j*) Y. Yang, N. Li, J. Miao, X. Cao, A. Ying, K. Pan, X. Lv, F. Ni, Z. Huang, S. Gong and C. Yang, *Angew. Chem., Int. Ed.*, 2022, **61**, e202202227.

10 (*a*) M. Grell, M. Oda, K. S. Whitehead, A. Asimakis, D. Neher and D. D. C. Bradley, *Adv. Mater.*, 2001, **13**, 577–580; (*b*) L. Wan, J. Wade, X. Shi, S. Xu, M. J. Fuchter and A. J. Campbell, *ACS Appl. Mater. Interfaces*, 2020, **12**, 39471–39478; (*c*) D. Tan, J. Dong, T. Ma, Q. Feng, S. Wang and D. T. Yang, *Angew. Chem., Int. Ed.*, 2023, **62**, e202304711; (*d*) P. Li, W. Li, Q. Lv, R. Chen and C. Zheng, *J. Mater. Chem. C*, 2023, **11**, 4033–4041.

11 (*a*) P. Ravat, R. Hinkelmann, D. Steinebrunner, A. Prescimone, I. Bodoky and M. Juricek, *Org. Lett.*, 2017, **19**, 3707–3710; (*b*) Y. Zhang, D. Zhang, T. Huang, A. J. Gillett, Y. Liu, D. Hu, L. Cui, Z. Bin, G. Li, J. Wei and L. Duan, *Angew. Chem., Int. Ed.*, 2021, **60**, 20498–20503; (*c*) J. M. dos Santos, D. Sun, J. M. Moreno-Naranjo, D. Hall, F. Zinna, S. T. J. Ryan, W. Shi, T. Matulaitis, D. B. Cordes, A. M. Z. Slawin, D. Beljonne, S. L. Warriner, Y. Olivier, M. J. Fuchter and E. Zysman-Colman, *J. Mater. Chem. C*, 2022, **10**, 4861–4870; (*d*) Y. Xu, Q. Wang, X. Song, Y. Wang and C. Li, *Chem.–Eur. J.*, 2023, **29**, e202203414.

12 (*a*) J. Barroso, J. L. Cabellos, S. Pan, F. Murillo, X. Zarate, M. A. Fernandez-Herrera and G. Merino, *Chem. Commun.*, 2018, **54**, 188–191; (*b*) M. Krzeszewski, H. Ito and K. Itami, *J. Am. Chem. Soc.*, 2022, **144**, 862–871; (*c*) J. Tan, X. Xu, J. Liu, S. Vasylevskyi, Z. Lin, R. Kabe, Y. Zou, K. Mullen, A. Narita and Y. Hu, *Angew. Chem., Int. Ed.*, 2023, **62**, e202218494.

13 (*a*) T. Katayama, S. Nakatsuka, H. Hirai, N. Yasuda, J. Kumar, T. Kawai and T. Hatakeyama, *J. Am. Chem. Soc.*, 2016, **138**,

5210–5213; (*b*) Y. Nakakuki, T. Hirose, H. Sotome, H. Miyasaka and K. Matsuda, *J. Am. Chem. Soc.*, 2018, **140**, 4317–4326; (*c*) J. L. Greenfield, J. Wade, J. R. Brandt, X. Shi, T. J. Penfold and M. J. Fuchter, *Chem. Sci.*, 2021, **12**, 8589–8602.

14 (*a*) Y.-F. Wu, L. Zhang, Q. Zhang, S.-Y. Xie and L.-S. Zheng, *Org. Chem. Front.*, 2022, **9**, 4726–4743; (*b*) G.-F. Huo, W.-T. Xu, Y. Han, J. Zhu, X. Hou, W. Fan, Y. Ni, S. Wu, H.-B. Yang and J. Wu, *Angew. Chem., Int. Ed.*, 2024, **63**, e202403149.

15 F. Zhang, F. Rauch, A. Swain, T. B. Marder and P. Ravat, *Angew. Chem., Int. Ed.*, 2023, **62**, e202218965.

16 (*a*) L. Yuan, Z.-L. Tu, J.-W. Xu, H.-X. Ni, Z.-P. Mao, W.-Y. Xu and Y.-X. Zheng, *Sci. China: Chem.*, 2023, **66**, 2612–2620; (*b*) G. Meng, J. Zhou, X. S. Han, W. Zhao, Y. Zhang, M. Li, C. F. Chen, D. Zhang and L. Duan, *Adv. Mater.*, 2024, **36**, 2307420; (*c*) W.-C. Guo, W.-L. Zhao, K.-K. Tan, M. Li and C.-F. Chen, *Angew. Chem., Int. Ed.*, 2024, **63**, e202401835.

17 Q. Wang, L. Yuan, C. Qu, T. Huang, X. Song, Y. Xu, Y.-X. Zheng and Y. Wang, *Adv. Mater.*, 2023, **35**, 2305125.

18 (*a*) Y. Zhang, D. Zhang, J. Wei, Z. Liu, Y. Lu and L. Duan, *Angew. Chem., Int. Ed.*, 2019, **58**, 16912–16917; (*b*) Y. Xu, Z. Cheng, Z. Li, B. Liang, J. Wang, J. Wei, Z. Zhang and Y. Wang, *Adv. Opt. Mater.*, 2020, **8**, 1902142; (*c*) M. Yang, I. S. Park and T. Yasuda, *J. Am. Chem. Soc.*, 2020, **142**, 19468–19472.

19 Y. Xu, C. Li, Z. Li, J. Wang, J. Xue, Q. Wang, X. Cai and Y. Wang, *CCS Chem.*, 2022, **4**, 2065–2079.

20 (*a*) A. Pershin, D. Hall, V. Lemaur, J.-C. Sancho-Garcia, L. Muccioli, E. Zysman-Colman, D. Beljonne and Y. Olivier, *Nat. Commun.*, 2019, **10**, 597; (*b*) S. Wu, W. Li, K. Yoshida, D. Hall, S. M. Suresh, T. Sayner, J. Gong, D. Beljonne, Y. Olivier, I. D. W. Samuel and E. Z.- Colman, *ACS Appl. Mater. Interfaces*, 2022, **14**, 22341–22352.

21 T. Lu and Q. Chen, *Theor. Chem. Acc.*, 2020, **139**, 25.

22 Z. Liu, T. Lu and Q. Chen, *Carbon*, 2020, **165**, 468–475.

23 (*a*) S. Grimme and S. D. Peyerimhoff, *Chem. Phys.*, 1996, **204**, 411–417; (*ab*) R. H. Janke, G. Haufe, E.-U. Würthwein and J. H. Borkent, *J. Am. Chem. Soc.*, 1996, **118**, 6031–6035.

24 T. Lu and Q. Chen, *Chem.: Methods*, 2021, **1**, 231–239.

25 (*a*) T. Otani, A. Tsuyuki, T. Iwachi, S. Someya, K. Tateno, H. Kawai, T. Saito, K. S. Kanyiva and T. Shibata, *Angew. Chem., Int. Ed.*, 2017, **56**, 3906–3910; (*b*) Y.-Y. Ju, L. Chai, K. Li, J.-F. Xing, X.-H. Ma, Z.-L. Qiu, X.-J. Zhao, J. Zhu and Y.-Z. Tan, *J. Am. Chem. Soc.*, 2023, **145**, 2815–2821.

26 L. Arrico, L. Di Bar and F. Zinna, *Chem.–Eur. J.*, 2021, **27**, 2920–2934.

27 Y. Xu, C. Li, Z. Li, Q. Wang, X. Cai, J. Wei and Y. Wang, *Angew. Chem., Int. Ed.*, 2020, **59**, 17442–17446.

28 (*a*) C. Murawski, K. Leo and M. C. Gather, *Adv. Mater.*, 2013, **25**, 6801–6827; (*b*) H. Nakanotani, T. Higuchi, T. Furukawa, K. Masui, K. Morimoto, M. Numata, H. Tanaka, Y. Sagara, T. Yasuda and C. Adachi, *Nat. Commun.*, 2014, **5**, 4016.